PAPER

Enhanced N₂ affinity of 1T-MoS₂ with a unique pseudo-six-membered ring consisting of N–Li–S–Mo–S–Mo for high ambient ammonia electrosynthesis performance†

Shivaraj B. Patil, [ID] ‡[a] Hung-Lung Chou,‡[b] Yu-Mei Chen,[a] Shang-Hsien Hsieh,[c] Chia-Hao Chen,[c] Chia-Che Chang,[a] Shin-Ren Li,[a] Yi-Cheng Lee,[a] Ying-Sheng Lin,[a] Hsin Li,[a] Yuan Jay Chang, [ID] [a] Ying-Huang Lai [ID] [a] and Di-Yan Wang [ID] *[a]

The Haber–Bosch process is widely used to convert atmospheric nitrogen (N₂) into ammonia (NH₃). However, the extreme reaction conditions and abundant carbon released by this process make it important to develop a greener NH₃ production method. The electrochemical nitrogen reduction reaction (NRR) is an attractive alternative to the Haber–Bosch process. Herein, we demonstrated that molybdenum sulfide on nickel foil (1T-MoS₂–Ni) with low crystallinity was an active NRR electrocatalyst. 1T-MoS₂–Ni achieved a high faradaic efficiency of 27.66% for the NRR at −0.3 V (*vs.* RHE) in a LiClO₄ electrolyte. *In situ* X-ray diffraction and *ex situ* X-ray photoemission analyses showed that lithium ions were intercalated into the 1T-MoS₂ layers during the NRR. Moreover, theoretical calculations revealed the differences between six membered rings formed in the 1T-MoS₂ and 2H-MoS₂ systems with Li intercalation. The bond distances of *d*(Mo–N) and *d*(N–Li) of in Li–1T-MoS₂ were found to be shorter than those in Li–2H-MoS₂, resulting in a lower energy barrier of N₂ fixation and higher NRR activity. Therefore, 1T-MoS₂–Ni is promising as a scalable and low-cost NRR electrocatalyst with lower power consumption and carbon emission than the Haber–Bosch process.

Introduction

Ammonia (NH₃) has attracted extensive interest for over a century because of its wide range of applications, including as a green fertilizer and non-carbon fuel for vehicles.[1–3] Although nitrogen (N₂) is the most abundant gas in the Earth's atmosphere, it is metabolically useless unless nitrogen fixation is carried out. The electrocatalytic nitrogen reduction reaction (NRR) is a promising process that breaks the triple bond of N₂ with suitable catalysts to form NH₃ (N₂ + 6H⁺ + 6e⁻ → 2NH₃).[4–7] There are three main factors that need to be considered to optimize electrocatalysts for the NRR: (1) the adsorption ability of N₂ on the catalyst surface, (2) reaction selectivity to suppress the hydrogen evolution reaction (HER), and (3) the compatibility and stability of materials.[8,9] It is important to develop new

catalysts that acceptably address these factors to realize highly efficient electrochemical N₂ reduction to NH₃.

Recently, many metal sulfides such as 2H-MoS₂,[10] FeS₂,[11] and SnS₂[12] have been investigated as catalysts for the NRR. However, metal sulfides show low faradaic efficiency (FE) in the NRR,[13–15] which has been attributed to poor N₂ adsorption on their surface and the inability to effectively suppress the HER. Understanding the detailed reaction mechanism of these catalysts could provide direction to design more active NRR catalysts. The electrochemical properties and reaction pathway of FeS₂ in the NRR were studied experimentally and by density functional theory (DFT) simulations.[11] The results showed that Fe atoms acted as NRR active centres and greatly lowered the energy barrier for the NRR. Sun *et al.*[16] revealed that Mo atoms were the NRR active centres of 2H-MoS₂, which displayed an FE of 1.2%. MoS₂ was decorated with Ru clusters to provide extra binding sites for N₂ activation for the NRR, resulting in an FE of 18%.[17]

Increasing catalyst surface activity through atomic manipulation is a promising direction to raise the FE of the electrochemical NRR. The preparation of metal oxides or sulfides with high metallic surface exposure to increase NRR activity has been proposed.[18] For example, Xin and co-workers achieved an FE of 14.6% (3.6 μg h⁻¹ mg_cat⁻¹) for atomically dispersed Mo atoms

[a]*Department of Chemistry, Tunghai University, Taichung 40704, Taiwan. E-mail: diyanwang@thu.edu.tw*

[b]*Graduate Institute of Applied Science and Technology, National Taiwan University of Science and Technology, Taipei 10607, Taiwan*

[c]*National Synchrotron Radiation Research Center, Hsinchu 30076, Taiwan*

1230 | *J. Mater. Chem. A*, 2021, **9**, 1230–1239

This journal is © The Royal Society of Chemistry 2021

on N-doped porous carbon.[19] The high FE and NH_3 yield of this catalyst were attributed to its high metal exposure, which facilitated N_2 adsorption.

It has also been found that low crystalline (amorphous) materials show enhanced NRR activity over their crystalline counterparts, which is attributed to the dangling bonds of low crystalline materials acting as unsaturated coordination sites for N_2 adsorption.[20] For example, Yan *et al.*[21] found that low crystalline Au on Ce_xO_2–reduced graphene oxide exhibited an FE of 10.10%, which was much higher than that of its crystalline counterpart (3.67%). The improved NRR activity was ascribed to the low crystalline structure providing more active sites for N_2 adsorption than the corresponding crystalline structure.

Recently, $1T\text{-}MoS_2$ has emerged as a promising material for a wide range of electrochemical applications because of its metallic properties and highly active surface, which is composed of a single layer of the S–Mo–S structure in which Mo is linked to six S atoms to form an octahedral lattice.[22–24] This structure endows $1T\text{-}MoS_2$ with abundant active sites and high electronic conductivity (six orders of magnitude higher than that of $2H\text{-}MoS_2$).[22] These characteristics facilitate the exclusive interactions of ions/molecules dissolved in an electrolyte with a $1T\text{-}MoS_2$ catalyst and the rapid diffusion of ions.[25] The dense active sites of $1T\text{-}MoS_2$ promote catalytic activity and its high electronic conductivity affords fast electron transfer.[24] Indeed, $1T\text{-}MoS_2$ has been used as an active catalyst for the HER.[22,23] To design an active $1T\text{-}MoS_2$ NRR electrocatalyst, its HER activity needs to be suppressed and the N_2 adsorption ability needs to be increased.

The NRR efficiency of $1T\text{-}MoS_2$ might be increased by forming new intermolecular interactions in the MoS_2 structure to facilitate N_2 adsorption. For example, the FE of $2H\text{-}MoS_2$ was increased by the formation of an additional Li–S bond in its

crystal structure during Li^+ intercalation.[25] The FE of this structure was 9.8%, which still has room for improvement. Because $1T\text{-}MoS_2$ has a different crystal structure from that of $2H\text{-}MoS_2$, it could form different intermolecular interactions with Li^+, which could modify its NRR catalytic activity. In this work, to further improve the NRR catalytic performance of $1T\text{-}MoS_2$, low crystalline $1T\text{-}MoS_2$ grown on nickel foil (denoted as $1T\text{-}MoS_2$–Ni) is designed as a robust electrocatalyst for the NRR. The performance of $1T\text{-}MoS_2$–Ni as an NRR electrocatalyst in a $LiClO_4$ electrolyte is investigated. *In situ* X-ray diffraction (XRD) and *ex situ* X-ray photoelectron spectroscopy (XPS) measurements are carried out to examine the intercalation of Li into $1T\text{-}MoS_2$. A detailed reaction pathway for Li-intercalated $1T\text{-}MoS_2$ ($Li\text{-}1T\text{-}MoS_2$) in the NRR is also elucidated.

Results and discussion

To study the differences between the catalytic mechanisms of N_2 reduction on the surface of $Li\text{-}1T\text{-}MoS_2$ and Li-intercalated $2H\text{-}MoS_2$ ($Li\text{-}2H\text{-}MoS_2$), model optimization was performed in $14 \times 14 \times 20$ Å^3 systems by DFT calculations, as shown in Fig. 1(a) and (b), respectively. The calculated N_2 adsorption energies at the Mo and S sites of the intrinsic $1T\text{-}MoS_2$ and Mo sites of $Li\text{-}1T\text{-}MoS_2$ and $Li\text{-}2H\text{-}MoS_2$ are listed in Table 1. The active site for N_2 adsorption on $1T\text{-}MoS_2$ is Mo because the Mo site possesses a negative N_2 adsorption energy (-0.28 eV). The N_2 adsorption energies on $Li\text{-}1T\text{-}MoS_2$ and $Li\text{-}2H\text{-}MoS_2$ were -0.72 and -0.70 eV, respectively, indicating their much stronger ability to adsorb N_2 than that of intrinsic $1T\text{-}MoS_2$. These results indicated that N_2 adsorption on the $1T\text{-}MoS_2$ or $2H\text{-}MoS_2$ surface was strongly affected by the specific interactions of Li and S atoms, which is consistent with the findings of a previous report.[26] To study the suppression of hydrogen
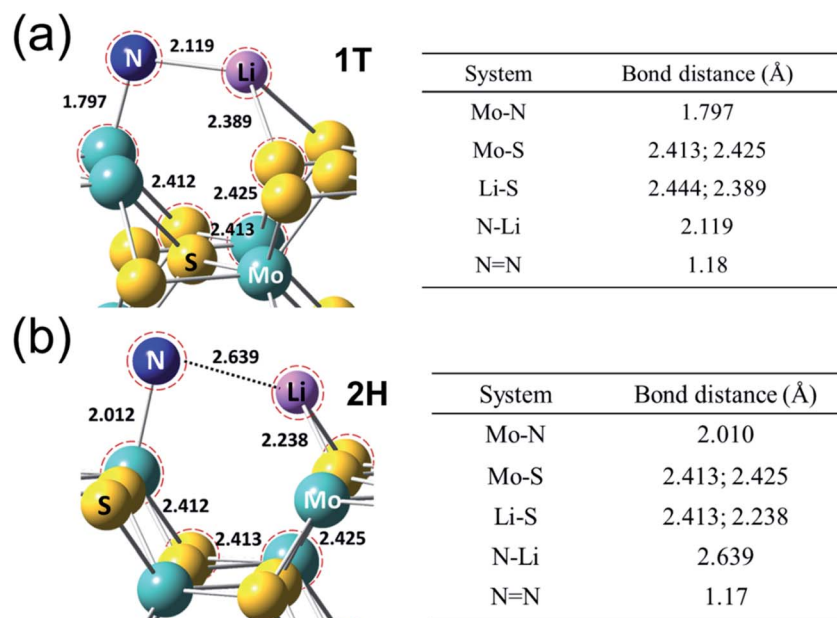

System	Bond distance (Å)
Mo-N	1.797
Mo-S	2.413; 2.425
Li-S	2.444; 2.389
N-Li	2.119
N=N	1.18

System	Bond distance (Å)
Mo-N	2.010
Mo-S	2.413; 2.425
Li-S	2.413; 2.238
N-Li	2.639
N=N	1.17

Fig. 1 The optimized configuration of the pseudo-six-member ring on (a) $1T\text{-}MoS_2$ and (b) $2H\text{-}MoS_2$ with Li−S interactions which consisted of the link of N···Li···S−Mo−S−Mo, respectively. The corresponding bond distances were provided on the right part of figures.

This journal is © The Royal Society of Chemistry 2021

J. Mater. Chem. A, 2021, **9**, 1230–1239 | **1231**

Table 1 Calculation of the adsorption energies and optimized geometries of N_2 in Li–1T-MoS_2 and Li–2H-MoS_2 systems

System	E_{ad} (eV)	Distance (Mo–N) (Å)	Distance (N–N) (Å)	Distance (Li–S) (Å)	Distance (Li–N) (Å)	Distance (Mo–S) (Å)
Mo site of 1T-MoS_2	−0.28	1.801	1.174			2.412; 2.424
S Site of 1T-MoS_2	+3.2					
Mo site of Li–1T-MoS_2	−0.72	1.797	1.181	2.444; 2.389	2.119	2.413; 2.425
Mo site of Li–2H-MoS_2	−0.70	2.010	1.172	2.413; 2.238	2.639	2.413; 2.425

adsorption on the S site in Li–1T-MoS_2, DFT calculation was also performed as shown in Table S1.† The results indicated that a hydrogen (H*) adsorption free energy (ΔG^{H*}) of 0.03 eV was obtained on the S-edge sites of the pristine MoS_2 system. In contrast, with Li–S interactions, the ΔG^{H*} increased dramatically to 0.49 eV on the S-edge sites of the Li–MoS_2 system. The result represented that S-edge sites in the pristine MoS_2 system were more favorable for the HER than that of Li–MoS_2 thermodynamically. Therefore, the Li–S bond can efficiently suppress the HER on the S atoms of MoS_2, which are believed to behave as the active sites for the HER.[16,26–29]

After geometry relaxation, the optimized calculated distance of N_2 in Li–1T-MoS_2 and Li–2H-MoS_2 (Fig. 1(a) and (b), respectively) showed that a pseudo-six-membered ring containing the interaction N···Li···S–Mo–S–Mo was formed. The N···Li interaction in the six-membered ring is believed to enhance the N_2 adsorption ability on the surface of MoS_2 and possibly weaken the N≡N bond to improve the conversion efficiency of the NRR.
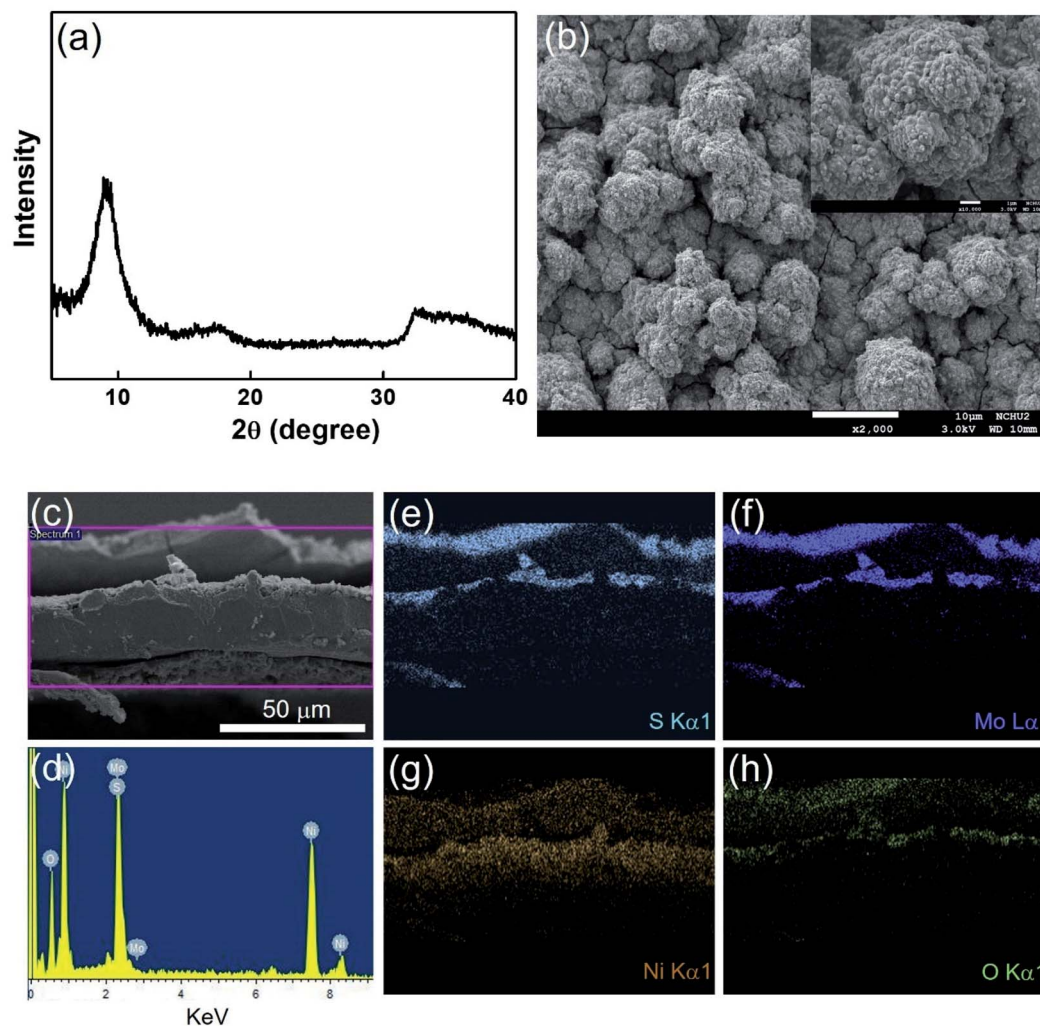

Fig. 2 (a) The XRD pattern of 1T-MoS_2–Ni. (b) The SEM image of 1T-MoS_2–Ni. The amplification image was shown in the inset. (c) Cross sectional SEM image and (d) related EDX spectrum of 1T-MoS_2–Ni. Elemental mapping of the (e) S atom, (f) Mo atom, (g) Ni atom and (h) O atom of 1T-MoS_2–Ni.

A comparison of the Li–1T-MoS$_2$ and Li–2H-MoS$_2$ systems revealed that the bond distances of d(Mo–N) of ~1.797 Å and d(N–Li) of ~2.119 Å in Li–1T-MoS$_2$ were shorter than d(Mo–N) of ~2.010 Å and d(N–Li) of ~2.639 Å in Li–2H-MoS$_2$, respectively. These results indicate that the N$_2$ adsorption ability of Li–1T-MoS$_2$ is stronger than that of Li–2H-MoS$_2$. In other words, the Li–1T-MoS$_2$ system should facilitate the formation of N–H bonds. Directed by these results, we fabricated and characterized Li–1T-MoS$_2$ as an NRR electrocatalyst.

Thiourea has been widely used as a sulfur source in the conventional synthesis of organic/inorganic compounds because of its high sulfur content, easy release of sulfur, and low cost, even though it is recognized as a toxic chemical. To make our catalyst fabrication as green and eco-friendly as possible, herein, 1T-MoS$_2$–Ni was fabricated by immersing pre-treated (acid-washed) Ni foil in a solution containing molybdic acid and a minimal amount of thiourea through a facile hydrothermal process. Fig. 2(a) shows the XRD pattern of 1T-MoS$_2$–Ni, which indicates that 1T-MoS$_2$–Ni has low crystallinity with two peaks at 9.0° and 18.72° corresponding to the (002) and (004) planes of 1T-MoS$_2$, respectively, in agreement with the literature.[30] These results were attributed to the formation of low crystalline 1T-MoS$_2$ on Ni foil. In contrast, 1T-MoS$_2$ grown on carbon fiber paper (1T-MoS$_2$–CFP) and 1T-MoS$_2$ grown on Ti foil (1T-MoS$_2$–Ti) displayed higher crystalline structures with peaks from the same planes observed in their XRD patterns (see the ESI†). Fig. S1(d) and (e)† show the Raman spectra of 1T-MoS$_2$ grown on different substrates and confirm the formation of 1T-MoS$_2$ with low crystallinity over Ni foil.[23,31,32] A scanning electron microscopy (SEM) image of 1T-MoS$_2$–Ni is shown in Fig. 2(b). It reveals that 1T-MoS$_2$–Ni consists of particles with rough surfaces. In contrast, 1T-MoS$_2$–CFP consisted of a sheet structure with high crystallinity (Fig. S2†). To analyze the elemental distribution of 1T-MoS$_2$–Ni, energy-dispersive X-ray spectroscopy (EDX) elemental mapping analysis was carried out. Fig. 2(c) shows a cross-sectional SEM image of 1T-MoS$_2$–Ni, which clearly illustrates that 1T-MoS$_2$ is attached to the Ni foil. Fig. 2(d)–(g) show the related EDX mapping of 1T-MoS$_2$–Ni, which confirmed the uniform distributions of Mo and S on Ni. The few signals from oxygen (Fig. 1(h)) could originate from the chemisorption of atmospheric oxygen.

To investigate the catalytic activity of 1T-MoS$_2$–Ni in the NRR, electrochemical experiments were conducted in N$_2$-saturated 0.25 M LiClO$_4$. The electrochemical reactions were carried out in an H-type cell in which the counter and working electrodes were separated by a Nafion membrane. Platinum wire (Pt) and a saturated calomel electrode (SCE) were used as counter and reference electrodes, respectively. All potentials are referenced to the reversible hydrogen electrode (RHE). Fig. 3(a) presents the results of linear sweep voltammetry (LSV) performed at a scan rate of 10 mV s^{-1} to determine the possible electrochemical window for the NRR over 1T-MoS$_2$–Ni. A current density of 10 mA cm^{-2} was obtained at an applied voltage of −0.6 V ($vs.$ RHE). To investigate the dependence of the electrochemical NRR with the 1T-MoS$_2$–Ni electrocatalyst on potential, constant–current curves were measured at different voltages of −0.2 to −0.6 V for 40 min, as shown in Fig. 3(b). The

current density increased from 2.0 to 10.0 mA cm^{-2} as the applied voltage changed from −0.2 to −0.6 V. Interestingly, no bubbles were observed in the range from −0.2 V to −0.6 V, meaning that hydrogen evolution on the surface of catalysts was suppressed substantially.

To detect and quantify the NH$_3$ formed during the electrocatalytic NRR over 1T-MoS$_2$–Ni at different potentials, indophenol was added as an indicator and measured by ultraviolet-visible (UV-vis) absorption spectroscopy. Fig. 3(c) shows the UV-vis absorption spectra of the electrolytes colored with indophenol. The results showed that the highest absorption intensity was around 0.40 a.u. at −0.3 V and the lowest was ~0.03 a.u. at −0.2 V. To further confirm the generation of NH$_3$ over the 1T-MoS$_2$–Ni electrocatalyst, ^{1}H nuclear magnetic resonance (NMR) spectra were obtained, as presented in Fig. 3(d). The sample for NMR measurements was produced using a mixture of ^{14}N$_2$ and ^{15}N$_2$ as the gas source in 0.25 M LiClO$_4$ at −0.3 V ($vs.$ RHE) for 4 h. The ^{1}H NMR spectrum clearly showed ^{14}NH$_4^+$ and ^{15}NH$_4^+$ signals, illustrating that NH$_3$ was produced by electrolysis over the 1T-MoS$_2$–Ni catalyst.

The NH$_3$ yields and related FE of 1T-MoS$_2$–Ni at given voltages are plotted in Fig. 3(e). At −0.2 V, the catalyst exhibited an FE of 11.57% and produced NH$_3$ at a rate of 0.11 μg min^{-1}, whereas it achieved its highest FE of 27.66% with an NH$_3$ yield rate of 1.05 μg min^{-1} cm^{-2} at −0.3 V. Beyond −0.3 V, the FE decreased at more negative potentials (8.02% at −0.4 V, 4.32% at −0.5 V, and 0.70% at −0.6 V). This phenomenon may be ascribed to the domination of the HER over the NRR at more negative potentials. The formation of hydrazine during the reaction was not detected (Fig. S3†). The Griess test of the electrolyte and gas chromatography of N$_2$ gas were also performed to check the NO$_x$ contamination and no contamination was found (Fig. S3 and S4†). Furthermore, controlled experiments were performed to show no effect of counter electrodes, anions of the salt and Ni foil on the NRR as shown in Fig. S5.†

To validate the effects of the 1T phase of 1T-MoS$_2$–Ni with low crystallite nature on its performance as an NRR electrocatalyst, 1T-MoS$_2$–CFP and 1T-MoS$_2$–Ti with highly crystalline structures were fabricated (Fig. S1 and S2†). In addition, 2H-MoS$_2$–CFP was also prepared by annealing 1T-MoS$_2$–CFP at high temperature in sulfur vapor. The structural characterization of 1T-MoS$_2$–CFP, 1T-MoS$_2$–Ti, and 2H-MoS$_2$–CFP is provided in the ESI.† All electrochemical tests were carried out in a 0.25 M LiClO$_4$ electrolyte at −0.3 V. Fig. 3(f) shows that 1T-MoS$_2$–CFP, 1T-MoS$_2$–Ti, and 2H-MoS$_2$–CFP with high crystallinity only achieved FEs of 12.24%, 10.5%, and 8.06%, respectively, in the NRR. These results confirm that the low crystallite nature of 1T-MoS$_2$–Ni leads to its high FE in the NRR by providing abundant active sites. Table S2† compares the performance of 1T-MoS$_2$–Ni with that of other reported metal sulfide NRR electrocatalysts.

To validate the stability of 1T-MoS$_2$–Ni, long term measurements and multiple cycles of the NRR were conducted. A long-term electrocatalytic NRR was carried out for 13 h at −0.3 V. Fig. 4(a) shows the time-dependent current curve of 1T-MoS$_2$–Ni at −0.3 V for 13 h. The corresponding absorption spectrum (inset of Fig. 3(a)) reveals that the absorption intensity of indophenol was 1.99 a.u. after 13 h. After 13 h of
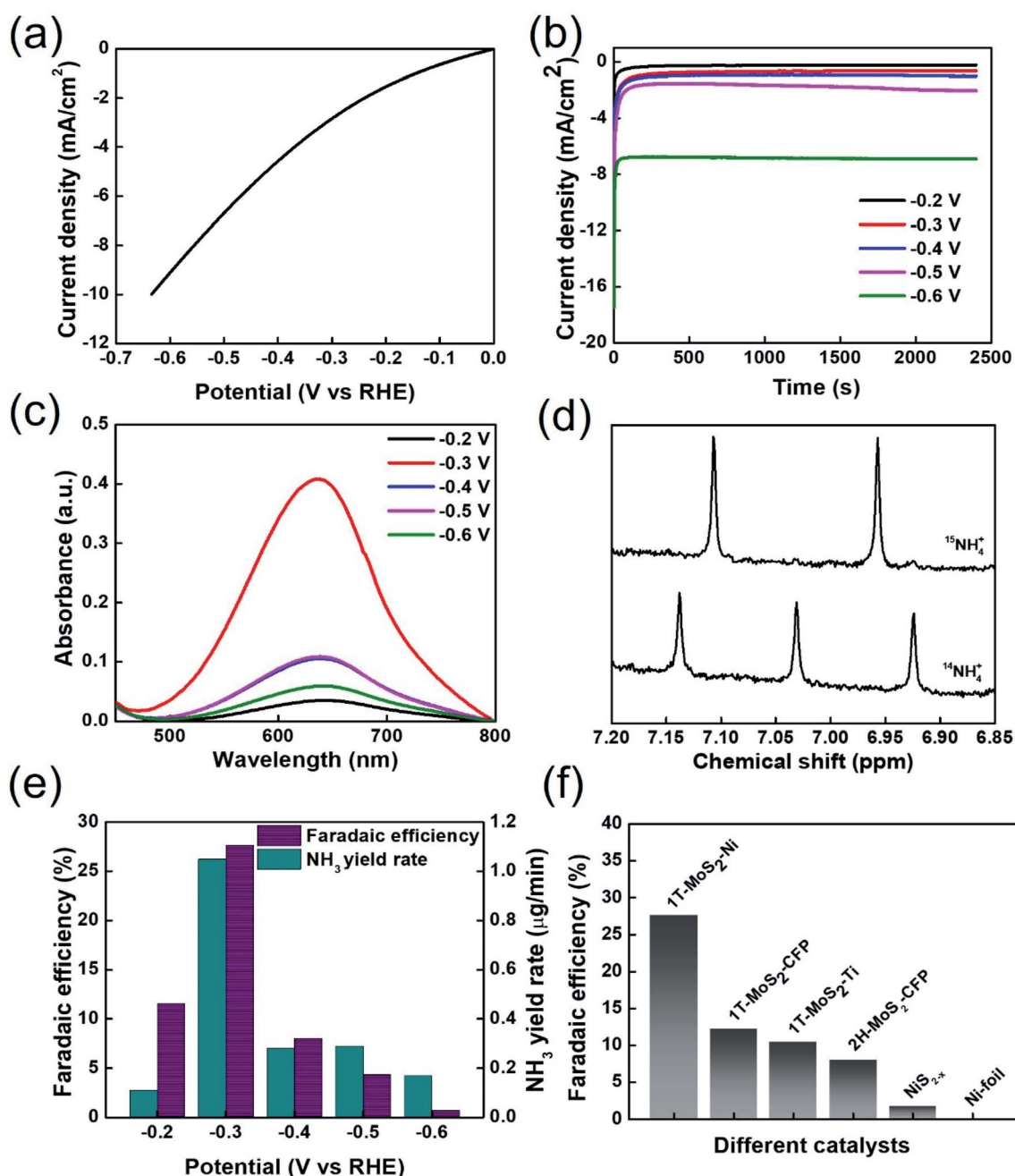
This journal is © The Royal Society of Chemistry 2021

J. Mater. Chem. A, 2021, **9**, 1230–1239 | **1233**

Fig. 3 (a) Linear sweep voltammetry of 1T-MoS$_2$–Ni operated in a N$_2$-saturated 0.25 M LiClO$_4$ electrolyte. (b) Time dependent current curves of 1T-MoS$_2$–Ni at different potentials (−0.2 to −0.6 V *vs.* RHE) in N$_2$-saturated 0.25 M LiClO$_4$. (c) UV-vis absorption spectra of the electrolytes colored with the indophenol indicator at a series of potentials for 40 min. (d) ^{1}H NMR spectrum of the yielded ^{15}NH$_4^+$ and ^{14}NH$_4^+$ after NRR electrolysis at −0.3 V using ^{15}N$_2$ and ^{14}N$_2$ as feeding gases, respectively. (e) Faradaic efficiency and respective NH$_3$ yield rate of 1T-MoS$_2$–Ni at different potentials. (f) Faradaic efficiency of different materials tested at −0.3 V in a 0.25 M LiClO$_4$ electrolyte.

electrocatalysis, the FE of 1T-MoS$_2$–Ni was still 26.47%. Fig. 4(b) displays the data obtained from consecutive electrochemical cycling tests. The NRR was conducted at −0.3 V for 40 min five times using the same 1T-MoS$_2$–Ni sample. Both the FE and NH$_3$ yield rate remained similar over the five cycles (corresponding time-dependent current curves and UV-vis spectra are provided in Fig. S6†). Overall, these results indicated that 1T-MoS$_2$–Ni demonstrated remarkably stable catalytic activity in the NRR.

The intercalation/interaction of Li$^+$ with MoS$_2$/S$_2^-$ has been recognized as another factor that can raise the NRR activity of 2H-MoS$_2$.[26] To investigate the Li$^+$ intercalation of 1T-MoS$_2$ during the electrochemical NRR in a LiClO$_4$ electrolyte, XPS and *in situ* XRD measurements were performed (see Fig. S7† for the *in situ* XRD setup). Intrinsic 1T-MoS$_2$ and 2H-MoS$_2$ with no Li intercalation were used as reference samples for comparison. Fig. 5(a)–(c) show Mo 3d, S 2p, and Li 1s spectra, respectively, for the samples.
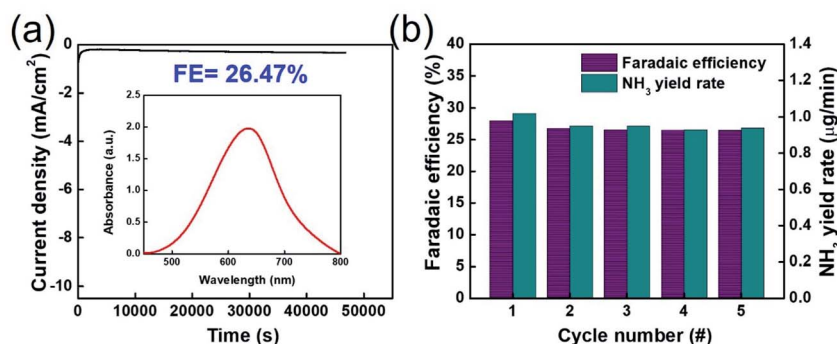
Fig. 4 (a) Time dependent current curves of 1T-MoS$_2$–Ni over 13 h (inset: UV-vis absorption spectra of the electrolyte stained with the indophenol indicator after NRR electrolysis for 13 h). (b) Faradaic efficiency and respective NH$_3$ yield rate of 1T-MoS$_2$–Ni for consecutive 5 cycles (40 min each).

Two characteristic peaks from Mo 3d$_{5/2}$ and Mo 3d$_{3/2}$ were clearly identified in the Mo 3d spectrum of MoS$_2$. These peaks of intrinsic 1T-MoS$_2$ were shifted to lower binding energy compared with those of 2H-MoS$_2$ (Fig. 5(a)). Similarly, the peaks ascribed to 2P$_{1/2}$ and 2P$_{3/2}$ in the S 2p spectrum of intrinsic 1T-MoS$_2$ were also shifted to lower binding energy compared with those of 2H-MoS$_2$ (Fig. 5(b)). The lower binding energies of Mo and S for intrinsic 1T-MoS$_2$ than for 2H-MoS$_2$ can be attributed to the increased electron density of the Mo and S atoms of 1T-MoS$_2$ compared with the case of 2H-MoS$_2$.[22,24,25,30,33,34] After electrolysis at −0.3 V for 40 min, the Mo 3d and S 2p peaks of 1T-MoS$_2$–Ni

slightly shifted to lower and higher energy, respectively, indicating that the oxidation state of S atoms of 1T-MoS$_2$–Ni was higher than that of intrinsic 1T-MoS$_2$. This result was attributed to the intercalation of Li$^+$ into 1T-MoS$_2$–Ni to form Li–1T-MoS$_2$–Ni, resulting in the formation of Li–S bonds.[26,34] Fig. 5(c) shows the rise of the Li 1s peak of Li–1T-MoS$_2$–Ni, further substantiating the intercalation of Li$^+$ into 1T-MoS$_2$.

Fig. 5(d) displays selected XRD patterns of 1T-MoS$_2$–CFP collected during the NRR in the LiClO$_4$ electrolyte with a linear scan from 0 to −0.6 V. We chose 1T-MoS$_2$–CFP for *in situ* XRD studies because its higher crystallinity than that of 1T-MoS$_2$–Ni
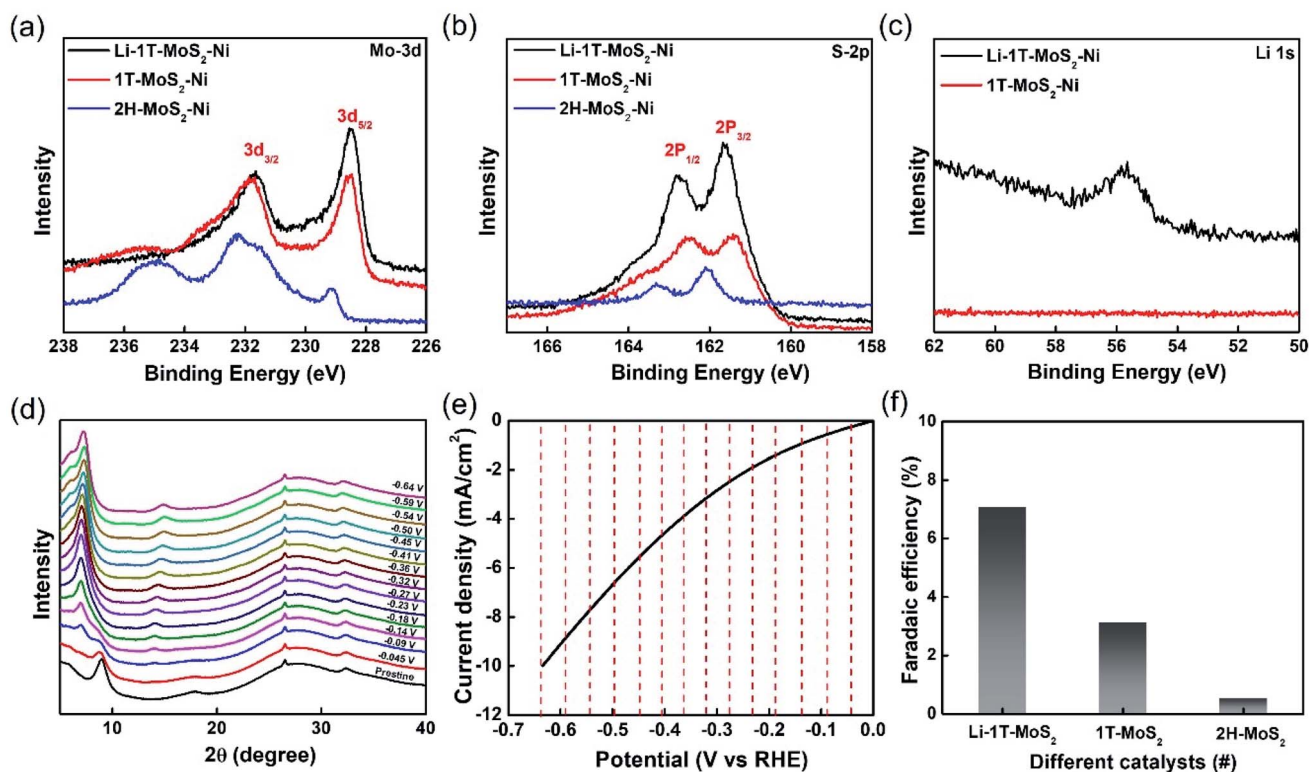

Fig. 5 (a) Mo-3d, (b) S-2p and (c) Li-1s XPS spectra of Li–1T-MoS$_2$–Ni, intrinsic 1T-MoS$_2$ and 2H-MoS$_2$, respectively. (d) *In situ* XRD patterns of representative 1T-MoS$_2$–CFP collected during the operation of the NRR in the LiClO$_4$ electrolyte with a scan rate of 0.5 mV from 0 to −0.6 V. (e) The corresponding linear scan voltammetry of 1T-MoS$_2$–CFP for *in situ* XRD measurement. The XRD spectra were collected from each voltage (red dashed line), as shown in Fig. 3(d). (f) Faradaic efficiency of different catalysts at −0.3 V in a 0.5 M Na$_2$SO$_4$ electrolyte.

facilitated the observation of its structural transformation. The corresponding linear scan is shown in Fig. 5(e). The results reveal that the peak observed at 9.5° for 1T-MoS$_2$ shifted to 7° at a more negative potential, confirming that Li$^+$ was intercalated into the 1T-MoS$_2$ layers.[35] To further study the effect of Li$^+$ on the NRR activity of Li–1T-MoS$_2$–Ni, Na$_2$SO$_4$ was used as the electrolyte in the NRR. Fig. 5(f) shows the FE of Li–1T-MoS$_2$–Ni, intrinsic 1T-MoS$_2$, and 2H-MoS$_2$ electrocatalysts operated in a 0.25 M NaSO$_4$ electrolyte at −0.3 V for 40 min. The corresponding current-dependent curves and UV-vis spectra are provided in Fig. S8.† Interestingly, Li–1T-MoS$_2$–Ni exhibited a higher FE compared with those of intrinsic 1T-MoS$_2$ and 2H-MoS$_2$. Furthermore, post catalytic characterization including XRD and SEM of 1T-MoS$_2$–Ni (Fig. S9†) revealed that the 1T phase with low crystallite nature remains unchanged. Owing to Li intercalation into the MoS$_2$ matrix, a shift of the dominant peak in XRD from 9° to 7° was also observed. Overall, these results confirmed the influence of Li$^+$ on the NRR activity of MoS$_2$. The role of Li$^+$ in increasing the FE of MoS$_2$ was further examined by DFT simulations.

To investigate the catalytic mechanism of Li–1T-MoS$_2$ in the NRR compared with those of intrinsic 1T-MoS$_2$ and Li-intercalated 2H-MoS$_2$ (Li–2H-MoS$_2$), DFT calculations were performed to determine their molecular structures and map potential energy diagrams of the NRR. In the models, N$_2$ was adsorbed on three kinds of MoS$_2$ slab surfaces consisting of one Li atom, 25 Mo atoms, and 46 S atoms, as shown in Fig. 6(a). The charge transfer between Mo, S, and Li atoms in Li–1T-MoS$_2$ was believed to be an important index that affects the adsorption ability of N$_2$ molecules and thus NRR activity. Fig. 6(b) presents the representative electron contour map of Li–1T-MoS$_2$ and the calculated charge transfer values are listed in Table 2. The formation of Li–S bonds was predicted in this model. Our results clearly showed that charge transfer occurred from Li to S in the Li–1T-MoS$_2$ system. The charge on S increased from 6.73e for intrinsic 1T-MoS$_2$ to 6.96e for Li–1T-MoS$_2$ and the charge on Li decreased from 3.61e for bare Li to 2.16e for Li–1T-MoS$_2$. Therefore, the charge of an N atom of N$_2$ increased from 6.87e to 6.98e upon adsorption by Li–1T-MoS$_2$, which could affect the bond strength of N$_2$ and facilitate the NRR.

Table 2 Bader charge analysis of N$_2$ adsorption on 1T-MoS$_2$ with Li–S interactions

Species	Charge (e)	Charge difference (e)
MoS$_2$	Mo: 4.70	
	S1: 6.80	
	S1: 6.80	
N$_2$	N: 6.87	
Li	L: 3.61	
1T-MoS$_2$ with Li	Mo (edge): 4.38	Mo (edge): 4.38 − 4.70 = −0.32
	S1 (edge): 6.90	S1 (edge): 6.90 − 6.80 = +0.10
	S2 (edge): 6.96	S2 (edge): 6.96 − 3.73 = +0.23
	Li: 2.16	Li: 2.16 − 3.61 = −1.45
	N: 6.98	N: 6.98 − 6.87 = +0.11

Fig. 7 shows the activation energy of the potential determining step for the NRR on intrinsic 1T-MoS$_2$, Li–1T-MoS$_2$, and Li–2H-MoS$_2$. For intrinsic 1T-MoS$_2$, an energy barrier of +0.79 eV was found for the reductive protonation of adsorbed N$_2$ (*NNH formation) without external potential. The energy barriers of the reductive protonation step for Li-intercalated 1T- and 2H-MoS$_2$ were much smaller than that for intrinsic 1T-MoS$_2$. In addition, the potentials of *NN adsorption (−0.72 eV) and *NNH formation (−0.23 eV) for Li–1T-MoS$_2$ were slightly lower than those for Li–2H-MoS$_2$ (−0.68 and −0.19 eV, respectively). In this step for the Li–1T-MoS$_2$ system, the N–N bond length increased from 1.18 Å in *N$_2$ to 1.23 Å *NNH. Therefore, the deformation charge density (Fig. 6(b)) clearly illustrated the charge transfer from N$_2$ to a positively charged Mo atom, resulting in the formation of an N–Mo bond and notable weakening of the N≡N triple bond and facilitating the intermediate protonation reaction to form *NNH. Indeed, the opening of the inert triple bond of N$_2$ was the most energetically demanding step of the NRR, which is logical. Overall, our results indicated that the Li–1T-MoS$_2$ catalyst demonstrated a relatively low energy barrier for the NRR, making it a promising electrocatalyst for this challenging but important reaction.
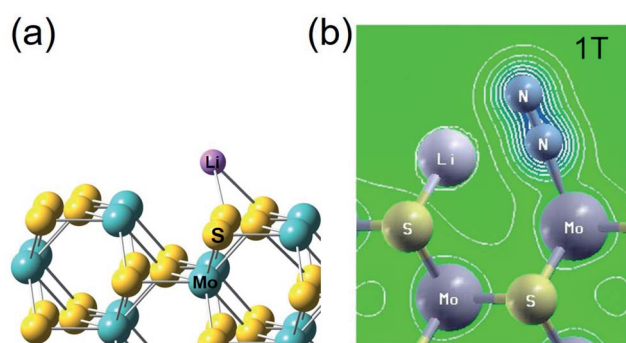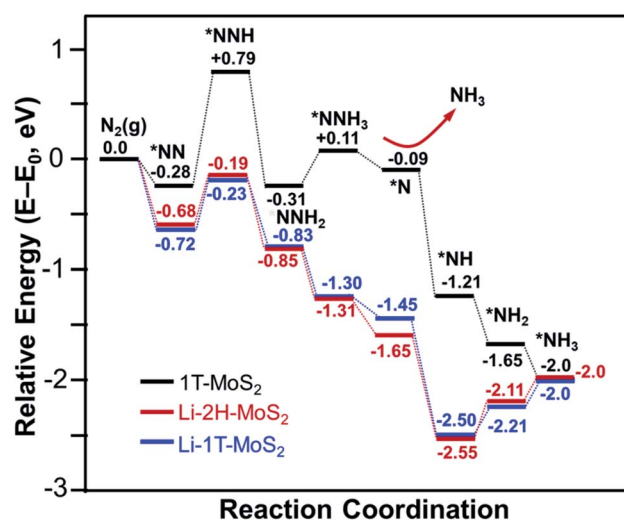

Fig. 6 (a) The models of the side view of the Li–1T-MoS$_2$ slab surface with the formation of a Li–S bond. (b) The representative electron contour map of intermediates N$_2$ adsorbed on the Mo atom of Li–1T-MoS$_2$.

Fig. 7 Potential energy diagram for the NRR at intrinsic 1T-MoS$_2$, Li–1T-MoS$_2$ and Li–2H-MoS$_2$. An asterisk (*) denotes an adsorption site.

1236 | J. Mater. Chem. A, 2021, **9**, 1230–1239

This journal is © The Royal Society of Chemistry 2021

Conclusion

We fabricated a high-performance $1T$-MoS_2–Ni electrocatalyst for the NRR with advantages including high exposure of metal active sites and high conductivity. The $1T$-MoS_2–Ni electrocatalyst achieved an FE of 27.66% and generated NH_3 at a rate of 1.05 µg min^{-1} cm^{-2} at −0.3 V in a 0.25 M $LiClO_4$ electrolyte. DFT calculations indicated the formation of a pseudo-six-membered ring with N_2 in the presence of Li^+, which not only lowered the energy barrier for N_2 fixation but also effectively suppressed the HER through strong Li–S interactions. This work provides fundamental insights into electrocatalyst fabrication and interfacial chemistry between the electrode and electrolyte, which may act as a blueprint for developing advanced NRR electrocatalysts in the future.

Materials

Molybdic acid (H_2MoO_4; ACS 85% min) and lithium perchlorate ($LiClO_4$; Analysis 99+%) were procured from Acros organics. Thiourea (CH_4N_2S; ACS 99+%), phenol (C_6H_5OH; ACS 100%), super P (ACS 99+%), Nafion (5 wt%) and titanium (Ti; 99.99%) foil were procured from Sigma-Aldrich. Sodium hydroxide (NaOH; ACS 97+%) was procured from Shimakyu's pure chemicals. Sodium hypochlorite (NaClO; 6–14% active Cl basis) and sodium sulfate (Na_2SO_4; ACS 99+%) were procured from Honeywell-Fluka. Sodium pentacyanonitrosylferrate(III) dihydrate ($Na_2[Fe(CN)_5NO]$· $2H_2O$; ACS 99+%) and lithium sulfate (Li_2SO_4; ACS 99.7%) were procured from Alfa Aesar. Nickel (Ni; 99.99%) foil was procured from MTI corporation, whereas carbon fiber paper (CFP) was procured from CeTech Co., Ltd. $^{14}N_2$ (5N) and $^{15}N_2$ (98 atom% ^{15}N) gases were procured from Toyo gas Co., Ltd., and Sigma-Aldrich, respectively. Distilled water and absolute ethanol were used throughout the experiments.

Fabrication of $1T$-MoS_2 nano-flowers

$1T$-MoS_2 nano-flowers were fabricated by adopting a simple hydrothermal method. Typically, 2.5 mM H_2MoO_4 and 6.25 mM CH_4N_2S were dissolved in 40 mL of distilled water and stirred vigorously for 30 min to form a homogeneous solution. The solution was then transferred to a Teflon-lined stainless-steel autoclave and sealed it. The autoclave was heated to 180 °C for 24 h and then cooled to room temperature. The obtained product was washed several times with DI water and ethanol. The resulting sample was dried at 60 °C to obtain a shiny black powder. The black powder was further characterized.

Fabrication of $1T$-MoS_2 on CFP, Ni and Ti foil

Similarly, $1T$-MoS_2 on CFP, Ni and Ti foil were synthesized by placing CFP, Ni and Ti foil into the autoclave, respectively, and maintaining all procedure unchanged. Finally, the samples were dried at 60 °C and stored in a desiccator.

Fabrication of the $1T$-MoS_2 electrode catalyst

$1T$-MoS_2 on Ni foil, CFP and Ti foil were used as it is by downsizing to a 1×2 cm^2 area. During the electrochemical measurements, it was immersed into the electrolyte with an area of 1×1 cm^2.

Characterization

XRD patterns were recorded by using an XRD instrument (Rigaku Miniflex 600). A JEOL JSM-7800F and JEOL 2100F were used to capture FESEM and HRTEM images, respectively. X-ray photoemission spectroscopy (XPS) measurements were performed at the SPEM end station (BL09A) of the National Synchrotron Radiation Research Center (NSRRC).[36] The photon energy used to obtain Mo 3d, S 2p and Li 1s XPS spectra was 320 eV. The in situ XRD measurement was performed with an electrochemical cell by the linear scan voltammetry method at a scan rate of 1 mV s^{-1}. The schematic setup is provided in the ESI.† In situ XRD analysis was performed at the beamline of BL23A small/wide angle X-ray scattering (SWAXS) at the Taiwan Light Source (TLS) and the beamline of 09A at the Taiwan Photon Source (TPS) at the National Synchrotron Radiation Research Center. Nuclear magnetic resonance (NMR) spectra were recorded using BRUKER Ascend TM 400 MHz.

Pretreatment prior to electrochemical measurements. Before each electrochemical measurement, all the units of the electrochemical cell were boiled and rinsed several times in DI water and dried at 100 °C. The Nafion membrane was used as received (no additional acid treatment). A new membrane was used for each measurement to avoid contamination. Furthermore, all the labware including vials, pipet, etc., was also rinsed with DI water several times. The $^{15}N_2$ and $^{14}N_2$ gases were passed through a saturator (0.05 M H_2SO_4) for high purity. Ar was purged for 30 min prior to $^{15}N_2$ flow to expel inherent $^{14}N_2$.[37,38]

Electrochemical setup and measurements. The nitrogen reduction reactions were performed in an H-cell under ambient conditions. It consists of two cells separated by a Nafion 211 membrane. The reference and working electrodes were placed in a single cell, whereas the counter electrode was placed in another cell. A CHI-660 electrochemical analyzer with a typical three electrode system was used to carry out all the electrochemical measurements. Herein, $1T$-MoS_2–Ni was devised as the working electrode, whereas a platinum rod (Pt) and saturated calomel electrode (SCE) were implemented as counter and reference electrodes, respectively. The potentials reported in this work were changed to the RHE scale with the following equation: E (vs. RHE) = E (vs. SCE) + 0.245 + 0.059 × pH. Subsequently, the current density was recorded with respect to the geometric surface area of the working electrode. N_2-saturated 0.25 M $LiClO_4$ was used as an electrolyte in this work. All experiments were carried out at room temperature.

Ammonia (NH_3) detection

The indophenol method with UV-vis spectroscopy was used to detect and quantify the yield amount of NH_3 in the solution. Briefly, 1 mL of electrolyte was collected from the cathodic cell and reacted with 100 µL of oxidizing solution containing NaClO (pCl = 6–14) in 1 M NaOH. It was followed by the addition of 100 µL of 0.5 M phenol and 50 µL of catalyst solution containing

0.002 M sodium nitropusside as the catalyst solution in turn. The solution mixture was mixed well gently for 30 s and kept still for 30 min under dark conditions. The absorbance measurements were recorded at $\lambda = 640$ nm. NH_3 concentration was quantified by using the concentration-absorbance calibration curve. Standard NH_4Cl solutions with NH_4^+ concentrations of 1, 2, 3, 4, 5, 6, 7, 8, 9, 10, 11, 12, 13, 14 and 15 μg mL^{-1} in 0.25 M $LiClO_4$ were used to calibrate the concentration-absorbance curve. The fitting curve ($y = 0.2952x + 0.008$; $R^2 = 0.9979$) was found to be in linear coherence with the concentration of NH_3 (Fig. S10†). Similarly, it was done for the Na_2SO_4 electrolyte also. The NMR method was also carried out to support the indophenol test results (Fig. S10†). The NMR calibration curve was obtained using an equimolar concentration of $^{14}NH_4^+$ and $^{15}NH_4^+$ as shown in Fig. S11.†

NH_3 yield rate (Y_{NH_3}) calculation

$$\text{Yield rate}_{mass} (NH_3) = (c(NH_3) \times V)/(t \times A) \qquad (1)$$

where $c(NH_3)$ is the measured concentration of NH_3, V is the volume of the electrolyte, t is the duration time of the reduction reaction, and A is the geometric area of the cathode (1×1 cm^2).

Faradaic efficiency (FE) calculation

Faradaic efficiency calculation in a 0.25 M $LiClO_4$ electrolyte was carried out assuming that one NH_3 molecule is produced with 3 electrons. It can be represented as follows:

$$FE = (3F \times C_{NH3} \times V)/(17 \times Q) \qquad (2)$$

where F stands for the faradaic constant (96 485 C mol^{-1}) and Q stands for the total quantity of supplied coulomb.

Hydrazine (N_2H_4) detection

The Watt and Chrisp method was adopted to quantify the N_2H_4 in the electrolyte after the reaction.[39] The coloring agent was prepared by mixing 5.99 g of *para*-(dimethylamino)benzaldehyde (p-$C_9H_{11}NO$) with 30 mL of hydrochloric acid (HCl) and 300 mL of ethanol (C_2H_5OH). Briefly, 9 mL of 1.0 M HCl was added to 1 mL of electrolyte (after the reaction) and was followed by the addition of 5 mL of coloring agent. The absorbance measurements were recorded at $\lambda = 455$ nm after incubating for 30 min.

^15N_2 isotope labeling studies

Using $^{15}N_2$ and $^{14}N_2$ as feeding gases, the ^{15}N and ^{14}N isotopic labeling studies were carried out, respectively. 99% enrichment of ^{15}N in $^{15}N_2$ was supplied by Sigma-Aldrich. The $^{15}N_2$ and $^{14}N_2$ gases were passed through a saturator (0.05 M H_2SO_4) for high purity. Briefly, electrocatalysis was carried out at 0.3 V for 4 h by continuously purging a saturated $^{15}N_2$ gas in the electrolyte (0.25 M $LiClO_4$). After the reaction, the reaction solution was concentrated to 2.0 mL at 80 °C for 3 h. The pH of the concentrated solution was adjusted to ~3 with adding some

0.01 M HCl. Then, 1 mL of the concentrated solution mixed with 0.2 mL of d6-DMSO was used for ^1H NMR spectroscopy measurement.

Theoretical calculations

In DFT calculations, we employed projector-augmented wave (PAW)[40,41] generalized gradient approximation (GGA).[42–44] In the plane wave calculations, a cutoff energy of 500 eV was applied, which was automatically set by the total energy convergence calculation for 1T-MoS_2 slab systems. DFT simulations were performed based on the unit cell of a 1T-MoS_2 system as shown in Fig. S12–S15.†[45] The dimensions of the unit cell are $a = b = 3.19$ Å, $c = 5.945$ Å^3, $\alpha = \beta = 90°$, and $\gamma = 120°$. Initially, 1T-MoS_2 was constructed to consist of a 1T-MoS_2 unit cell structure containing one Mo atoms with one S atoms; the system was then allowed to reach its lowest energy configuration by a relaxation procedure. For these calculations, a $3 \times 3 \times 1$ k-point mesh was used in the super cell. The atoms in the cell were allowed to relax until the forces on unconstrained atoms are less than 0.01 eV Å^{-1}. The adsorption energy in the N_2–1T-MoS_2 system, E_{ad}, is defined as the sum of interactions between the capping molecule and slab system, and it is given as $E_{ad} = E_{total} - E_{MoS_2} - (E_{N_2})$, where E_{total}, E_{MoS_2} and E_{N_2} are the total energy of the system, the 1T-MoS_2 system energy, and the single N_2 molecule energy. The negative sign of E_{ad} corresponds to the energy gain of the system due to molecular adsorption.

Author contributions

S. Patil and D. Wang conceived the project and designed the experiments. S. Patil, Y. Chen, C. Chang, S. Li, Y. Lee and Y. Lai performed material preparation, structural characterization and electrochemical measurements. S. Hsieh and C. Chen helped to perform the X-ray photoemission measurement in the NSRRC. H. Chou helped to perform DFT simulation. Y. Lin, Hsin Li and Y. Chang helped to do NMR measurements. S. Patil and D. Wang co-wrote the paper. All authors discussed the results and commented on the manuscript.

Conflicts of interest

The authors declare no conflict of interest.

Acknowledgements

References

1 T. Oshikiri, K. Ueno and H. Misawa, *Angew. Chem., Int. Ed.*, 2016, **55**, 3942–3946.

1238 | *J. Mater. Chem. A*, 2021, **9**, 1230–1239

This journal is © The Royal Society of Chemistry 2021

2 V. Rosca, M. Duca, M. T. de Groot and M. T. Koper, *Chem. Rev.*, 2009, **109**, 2209–2244.

3 R. F. Service, *Science*, 2014, **345**, 610.

4 C. Guo, J. Ran, A. Vasileff and S.-Z. Qiao, *Energy Environ. Sci.*, 2018, **11**, 45–56.

5 X. Cui, C. Tang and Q. Zhang, *Adv. Energy Mater.*, 2018, **8**, 1800369.

6 Z. Yan, M. Ji, J. Xia and H. Zhu, *Adv. Energy Mater.*, 2019, 1902020.

7 Y.-C. Hao, Y. Guo, L.-W. Chen, M. Shu, X.-Y. Wang, T.-A. Bu, W.-Y. Gao, N. Zhang, X. Su and X. Feng, *Nat. Catal.*, 2019, **2**, 448–456.

8 S. Dou, X. Wang and S. Wang, *Small Methods*, 2019, **3**, 1800211.

9 G. F. Chen, S. Ren, L. Zhang, H. Cheng, Y. Luo, K. Zhu, L. X. Ding and H. Wang, *Small Methods*, 2019, **3**, 1800337.

10 J. Zhang, X. Tian, M. Liu, H. Guo, J. Zhou, Q. Fang, Z. Liu, Q. Wu and J. Lou, *J. Am. Chem. Soc.*, 2019, **141**, 19269–19275.

11 C. C. Chang, S. R. Li, H. L. Chou, Y. C. Lee, S. Patil, Y. S. Lin, C. C. Chang, Y. J. Chang and D. Y. Wang, *Small*, 2019, **15**, 1904723.

12 P. Li, W. Fu, P. Zhuang, Y. Cao, C. Tang, A. B. Watson, P. Dong, J. Shen and M. Ye, *Small*, 2019, **15**, 1902535.

13 K. C. MacLeod and P. L. Holland, *Nat. Chem.*, 2013, **5**, 559.

14 X. Guo, H. Du, F. Qu and J. Li, *J. Mater. Chem. A*, 2019, **7**, 3531–3543.

15 S. B. Patil and D. Y. Wang, *Small*, 2020, 2002885.

16 L. Zhang, X. Ji, X. Ren, Y. Ma, X. Shi, Z. Tian, A. M. Asiri, L. Chen, B. Tang and X. Sun, *Adv. Mater.*, 2018, **30**, 1800191.

17 B. H. Suryanto, D. Wang, L. M. Azofra, M. Harb, L. Cavallo, R. Jalili, D. R. Mitchell, M. Chatti and D. R. MacFarlane, *ACS Energy Lett.*, 2018, **4**, 430–435.

18 Y. Qiu, X. Peng, F. Lü, Y. Mi, L. Zhuo, J. Ren, X. Liu and J. Luo, *Chem.–Asian J.*, 2019, **14**, 2770–2779.

19 L. Han, X. Liu, J. Chen, R. Lin, H. Liu, F. Lü, S. Bak, Z. Liang, S. Zhao and E. Stavitski, *Angew. Chem.*, 2019, **131**, 2343–2347.

20 M. M. Shi, D. Bao, S. J. Li, B. R. Wulan, J. M. Yan and Q. Jiang, *Adv. Energy Mater.*, 2018, **8**, 1800124.

21 S. J. Li, D. Bao, M. M. Shi, B. R. Wulan, J. M. Yan and Q. Jiang, *Adv. Mater.*, 2017, **29**, 1700001.

22 X. Geng, W. Sun, W. Wu, B. Chen, A. Al-Hilo, M. Benamara, H. Zhu, F. Watanabe, J. Cui and T.-p. Chen, *Nat. Commun.*, 2016, **7**, 1–7.

23 M. A. Lukowski, A. S. Daniel, F. Meng, A. Forticaux, L. Li and S. Jin, *J. Am. Chem. Soc.*, 2013, **135**, 10274–10277.

24 M. Acerce, D. Voiry and M. Chhowalla, *Nat. Nanotechnol.*, 2015, **10**, 313.

25 J. He, G. Hartmann, M. Lee, G. S. Hwang, Y. Chen and A. Manthiram, *Energy Environ. Sci.*, 2019, **12**, 344–350.

26 Y. Liu, M. Han, Q. Xiong, S. Zhang, C. Zhao, W. Gong, G. Wang, H. Zhang and H. Zhao, *Adv. Energy Mater.*, 2019, **9**, 1803935.

27 C. Tsai, H. Li, S. Park, J. Park, H. S. Han, J. K. Nørskov, X. Zheng and F. Abild-Pedersen, *Nat. Commun.*, 2017, **8**, 1–8.

28 B. Seo and S. H. Joo, *Nano Convergence*, 2017, **4**, 1–11.

29 C.-H. Lee, S. Lee, Y.-K. Lee, Y. C. Jung, Y.-I. Ko, D. C. Lee and H.-I. Joh, *ACS Catal.*, 2018, **8**, 5221–5227.

30 T. Xiang, Q. Fang, H. Xie, C. Wu, C. Wang, Y. Zhou, D. Liu, S. Chen, A. Khalil and S. Tao, *Nanoscale*, 2017, **9**, 6975–6983.

31 N. H. Attanayake, A. C. Thenuwara, A. Patra, Y. V. Aulin, T. M. Tran, H. Chakraborty, E. Borguet, M. L. Klein, J. P. Perdew and D. R. Strongin, *ACS Energy Lett.*, 2017, **3**, 7–13.

32 D. Yang, S. J. Sandoval, W. Divigalpitiya, J. Irwin and R. Frindt, *Phys. Rev. B: Condens. Matter Mater. Phys.*, 1991, **43**, 12053.

33 Y. Li, H. Wang, L. Xie, Y. Liang, G. Hong and H. Dai, *J. Am. Chem. Soc.*, 2011, **133**, 7296–7299.

34 L. Wu, N. Y. Dzade, M. Yu, B. Mezari, A. J. van Hoof, H. Friedrich, N. H. de Leeuw, E. J. Hensen and J. P. Hofmann, *ACS Energy Lett.*, 2019, **4**, 1733–1740.

35 C. D. Quilty, L. M. Housel, D. C. Bock, M. R. Dunkin, L. Wang, D. M. Lutz, A. Abraham, A. M. Bruck, E. S. Takeuchi and K. J. Takeuchi, *ACS Appl. Energy Mater.*, 2019, **2**, 7635–7646.

36 H.-J. Liao, Y.-M. Chen, Y.-T. Kao, J.-Y. An, Y.-H. Lai and D.-Y. Wang, *J. Phys. Chem. C*, 2017, **121**, 24463–24469.

37 S. Z. Andersen, V. Čolić, S. Yang, J. A. Schwalbe, A. C. Nielander, J. M. McEnaney, K. Enemark-Rasmussen, J. G. Baker, A. R. Singh and B. A. Rohr, *Nature*, 2019, **570**, 504–508.

38 C. Li, S. Mou, X. Zhu, F. Wang, Y. Wang, Y. Qiao, X. Shi, Y. Luo, B. Zheng and Q. Li, *Chem. Commun.*, 2019, **55**, 14474–14477.

39 G. W. Watt and J. D. Chrisp, *Anal. Chem.*, 1952, **24**, 2006–2008.

40 D. Vanderbilt, *Phys. Rev. B: Condens. Matter Mater. Phys.*, 1990, **41**, 7892.

41 M. C. Payne, M. P. Teter, D. C. Allan, T. Arias and a. J. Joannopoulos, *Rev. Mod. Phys.*, 1992, **64**, 1045.

42 J. P. Perdew, J. A. Chevary, S. H. Vosko, K. A. Jackson, M. R. Pederson, D. J. Singh and C. Fiolhais, *Phys. Rev. B: Condens. Matter Mater. Phys.*, 1992, **46**, 6671.

43 G. Kresse and J. Hafner, *Phys. Rev. B: Condens. Matter Mater. Phys.*, 1996, **54**, 11169.

44 G. Kresse and D. Joubert, *Phys. Rev. B: Condens. Matter Mater. Phys.*, 1999, **59**, 1758.

45 T. Hu, R. Li and J. Dong, *J. Chem. Phys.*, 2013, **139**, 174702.

This journal is © The Royal Society of Chemistry 2021

J. Mater. Chem. A, 2021, **9**, 1230–1239 | **1239**